Materials Advances

ROYAL SOCIETY OF CHEMISTRY

PAPER

View Article Online
View Journal | View Issue

Check for updates

Cite this: *Mater. Adv.*, 2025, **6**, 607

Engineering carbonyl-rich conjugated microporous polymers with a pyrene-4,5,9,10-tetraone building block as highly efficient and stable electrodes for energy storage†

Ahmed F. Saber,[a] Ya-Fan Chen,[b] Levannie Mabuti,[b] Swetha V. Chaganti,[c] Santosh U. Sharma,[c] Johann Lüder,[b] Jyh-Tsung Lee,[c] Shiao-Wei Kuo[b] and Ahmed F. M. EL-Mahdy*[bd]

Received 15th September 2024,
Accepted 26th November 2024

DOI: 10.1039/d4ma00928b

rsc.li/materials-advances

As a solution to the environmental and energy crises, more safe and efficient energy storage technologies are extremely necessary. Conjugated microporous polymers (CMPs) bearing redox-active functional groups as well as nitrogen-rich moieties have received a lot of interest in energy conversion and storage applications. Herein, two novel redox-active pyrene-4,5,9,10-tetraone-based CMPs, BC-PT and TPA-PT, were successfully fabricated *via* Suzuki coupling of 2,7-dibromopyrene-4,5,9,10-tetraone (PT-2Br) with 3,3′,6,6′-tetrakis(4,4,5,5-tetramethyl-1,3,2-dioxaborolan-2-yl)-9,9′-bicarbazole (BC-4BO) and N^1,N^1,N^4,N^4-tetrakis(4-(4,4,5,5-tetramethyl-1,3,2-dioxaborolan-2-yl)phenyl)benzene-1,4-diamine (TPA-4BO), respectively. Their chemical composition, porosity parameters, morphological structures, and thermal behavior were investigated. In three-electrode supercapacitors, the electrochemical behavior showed that BC-PT CMP exhibited the top specific capacitance of 373 F g^{-1} in aqueous KOH (1.0 M) at a current density of 1.0 A g^{-1}. It also possessed a great cyclability maintaining 94.37% of primary capacitance at 10 A g^{-1} current density even after 5000 GCD cycles. A two-electrode supercapacitor with the BC-PT CMP displayed a superb electrochemical capacitance of 107 F g^{-1} at 1.2 A g^{-1}, a greater retention of 97.69% over 5000 GCD cycles at 10 A g^{-1}, and a better energy density of 14.86 W h kg^{-1}. The excellent efficiency of BC-PT CMP compared to that of TPA-PT CMP can be explained in terms of high specific surface area (478 m^2 g^{-1}), large pore volume (0.44 cm^3 g^{-1}), great planarity, and better conductivity. Accordingly, BC-PT CMP is a prospective candidate for storing energy. Besides the novelty of our synthesized polymers, they exhibited outstanding electrochemical characteristics, both in three-electrode and two-electrode systems, which were comparable to those of many other polymers.

Introduction

The big need and endeavor for renewable energy sources, such as solar energy, biomass energy, and geothermal energy have increased considerably. Owing to factors such as time, geographic nature, and seasons, renewable energy sources vary to a large extent; therefore, the discovery of permanent systems for storing energy has become highly necessary. As a result, fuel cells, batteries, traditional capacitors, and supercapacitors are being constructed to provide dynamic alternatives for both storing and transferring electrical energy.[1–6] One of the more efficient devices among various energy storage systems is supercapacitors (SCs), which are considered important alternatives for storing energy because of their outstanding characteristics (*i.e.*, safety, cheapness, long lifetime, fast charge/discharge time, lower resistance, and higher power density) in comparison to other individual and hybrid techniques.[7–11] The important criteria for selecting an electrode to be applied as an efficient material for SCs is their ability to store electrical charges through one of the two major mechanisms (electrical double-layer capacitance (EDLC) and pseudocapacitance). Polymer-based SCs are pivotal materials in building of many

---

[a] *Interdisciplinary Research Center for Hydrogen Technologies and Carbon Management (IRCHTCM), King Fahd University of Petroleum & Minerals, Dhahran 31261, Saudi Arabia*
[b] *Department of Materials and Optoelectronic Science, National Sun Yat-Sen University, Kaohsiung 80424, Taiwan*
[c] *Department of Chemistry, National Sun Yat-Sen University, Kaohsiung 80424, Taiwan*
[d] *Chemistry Department, Faculty of Science, Assiut University, Assiut 71516, Egypt*

† Electronic supplementary information (ESI) available. See DOI: https://doi.org/10.1039/d4ma00928b

energy storage devices with higher power energy.[12] Accordingly, porous organic polymers (POPs) with the merits of porous structure, extended conjugation, and nitrogen-rich network are most preferred for application as promising SC electrodes.[13]

POPs consist of many sub-divided categories, including conjugated microporous polymers (CMPs), covalent organic frameworks (COFs), and hypercrosslinked polymers (HCPs), that have been constructed *via* different synthetic mechanisms with tunable properties for a wide spectrum of applications.[14–16] Among them, CMPs have aroused great attention due to their conjugated skeleton, permanent porosity, and outstanding semiconductor characteristics.[17,18] They are prepared through various conventional polymerization approaches, such as Sonogashira,[19–21] Suzuki,[22–24] Yamamoto,[25–27] Schiff-base,[28,29] oxidative,[30] and phenazine ring-fusion[31–33] reactions. The combination of CMPs with other materials such as nanoarchitectures, organic frameworks, and porous and colloidal materials can yield smart substances for energy storage applications.[34–36] Furthermore, CMPs can be applied in gas uptake,[37] light harvesting,[38] sensing,[39] dye adsorption,[40] catalysis,[41] and supercapacitors.[42]

Pyrene-4,5,9,10-tetraone (PT) as a redox-active unit was first synthesized by the Harris group *via* a one-step chemical reaction of pyrene, ruthenium chloride catalyst, and sodium periodate as an oxidant material.[43] PT with cyclic 1,2-diketones structure, which holds four active carbonyl groups is electrically more efficient than the corresponding acyclic 1,2-diketone as organic electrode materials.[44] These carbonyl functional groups in PT integrate the stability of the polymers after discharging owing to the adjacency in configuration, connection to aromatics, and high conjugation upon reduction.[45] Many POP materials with PT linkage have been designed and prepared for both lithium and sodium batteries and secondary batteries.[46,47]

It is an effective strategy to incorporate the PT unit along with bicarbazole (BC) or triphenylamine (TPA) nitrogen-rich units into an extended conjugation system to improve the conductivity and obtain highly efficient polymeric electrodes for SCs. The resulting polymer will have donor–acceptor (D–A) characteristics since PT has electron-deficient properties, whereas BC and TPA are electron donors. The D–A type polymers exhibit low band gaps, which endow the polymers with higher conductivity and lower electrode potential making them very suitable as electrode materials.

In this study, we constructed two D–A type CMPs on the strength of PT containing abundant carbonyl groups, linked together with either BC or TPA monomers through C–C bond linkage using one-step polycondensation Suzuki coupling and employing them for SCs application (Scheme 1). The chemical composition, thermal degradation temperatures, porosity parameters, and morphological structure of the obtained redox-active CMPs were investigated through various methods including Fourier transform infrared (FTIR), thermal gravimetric analysis (TGA), X-ray photoelectron spectroscopy (XPS), nuclear magnetic resonance (NMR), Brunauer–Emmett–Teller (BET), X-ray diffraction (XRD), scanning electron microscopy (SEM), and transmission electron microscopy (TEM). Owing to the presence of a redox-active unit (PT) in our synthesized polymers, cyclic voltammetry (CV) and galvanostatic charge–discharge (GCD) techniques have been applied and the obtained data showed that both BC-PT and TPA-PT CMPs had excellent specific capacitance with great stability compared to other polymeric electrode materials.

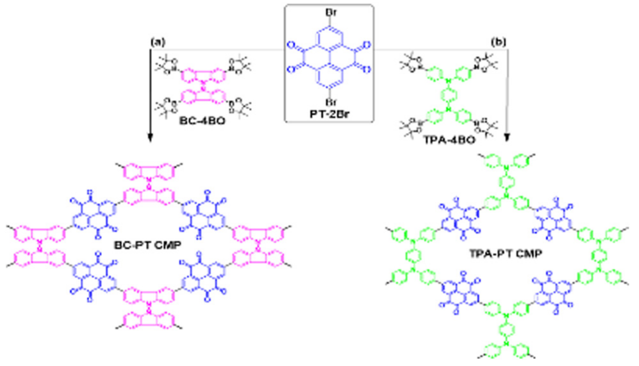

Scheme 1 Synthesis of (a) BC-PT CMP and (b) TPA-PT CMP.

Results and discussion

In the presented research, we synthesized two novel D–A conjugated polymers namely: BC-PT and TPA-PT CMPs containing the pyrene-4,5,9,10-tetraone (PT) unit with many redox-active carbonyls *via* a simple and efficient Suzuki polymerization reaction. The BC-PT and TPA-PT polymers were constructed as dark-colored powders *via* the chemical condensation of the PT-2Br major monomer with BC-4BO and TPA-4BO, respectively, in the H_2O/DMF co-solvent, in the presence of $Pd(PPh_3)_4$ catalyst at 145 °C for 72 h (Scheme 1). The applied PT-2Br, BC-4BO, and TPA-4BO monomers were synthesized according to the literature[48,49] (Schemes S1–S3, ESI†).

FTIR and solid-state ^{13}C cross-polarization magic angle spinning nuclear magnetic resonance (^{13}C CP/MAS NMR) spectroscopic techniques were utilized to assess the as-synthesized polymeric structures. As outlined in (Fig. 1a and Fig. S1 and S2, ESI†), the full disappearance of B–O and C–H vibrational frequencies in the FTIR spectrum of PT-based CMPs compared with the spectra of its precursors BC-4BO (1350, 2977 and 2930 cm^{-1}) and TPA-4BO (1358, 2973 and 2930 cm^{-1}), as well as the vanishing of the C–Br absorption band located at 723 cm^{-1} for PT-2Br demonstrated a successful C–C coupling of monomers leading to polymers. Also, the FTIR spectrum of BC-PT CMP exhibited the characteristic peaks of the C=C, C=O, and C–H aromatic stretching bonds at 1604, 1678, and 3058 cm^{-1}, respectively, whereas those for TPA-PT CMP were centered at 1594, 1678, and 3031 cm^{-1}, respectively, which were slightly shifted in comparison to the starting monomers confirming the complete formation of the polymeric materials.

In addition, the chemical composition of the prepared CMPs was supported by the solid-state ^{13}C CP/MAS NMR spectra, in which characteristic peaks at 192.24 and 190.90 ppm were observed for BC-PT and TPA-PT CMPs, respectively, which were attributed to C=O bonds. Moreover, broad peaks located in the

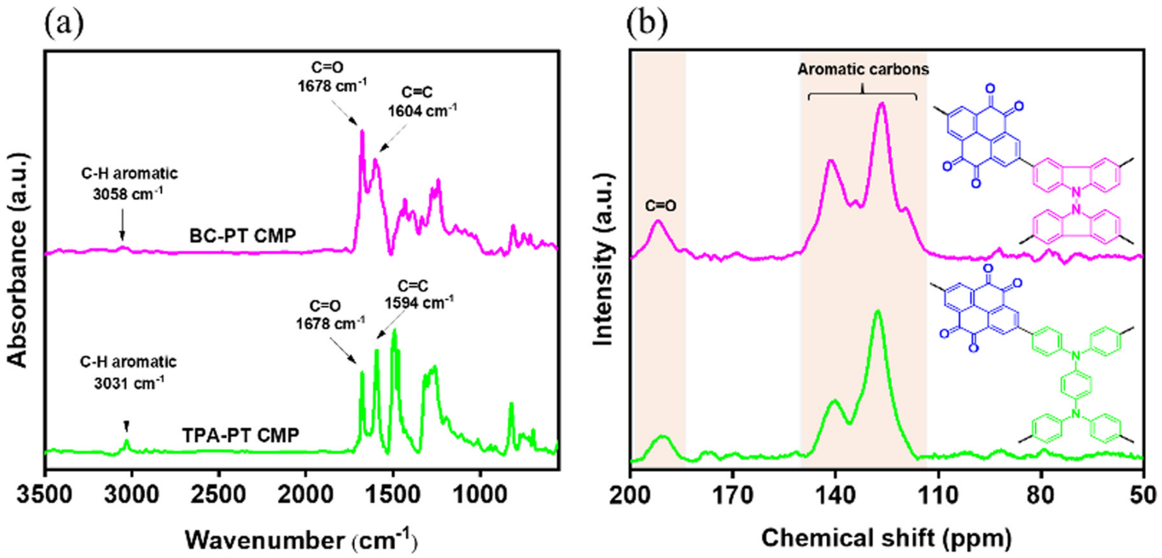

Fig. 1 (a) FTIR, and (b) solid-state ^{13}C CP/MAS NMR spectra of BC-PT, and TPA-PT CMPs.

range 114.84–149.04 ppm for BC-PT CMP, and in the range 118.33–146.68 ppm for TPA-PT CMP were assigned to the aromatic carbons. The missing signals in the range of 20–90 ppm suggest that the B–O and C–Br bonds of the starting precursors have been consumed (Fig. 1b).

Thermal stabilities of the PT-linked CMPs were determined using TGA in a nitrogen stream at 20 °C min^{-1}. According to (Fig. S3, ESI†), there is a clear decline in the thermal curves for both of them owing to the weight loss at higher temperatures. TGA analysis provided that the temperature of 10% weight loss (T_{d10}) and char yield values for BC-PT CMP were 443 °C and 73%, respectively, whereas the values were measured to be 424 °C and 74% for TPA-PT CMP, respectively. From the data obtained, one can conclude that our porous polymers had considerable thermal stability (Table S1, ESI†). It was observed that the obtained polymers had very poor solubility in almost all organic solvents (MeOH, EtOH, DMF, NMP, THF, and acetone) indicating significant cross-linking frameworks due to high polymerization degree (Fig. S4, ESI†).

Fig. 2a and e show the XPS results conducted on the synthesized polymers, which consisted of C, N and O elements. The BC-PT polymer possessed three XPS signals characteristic

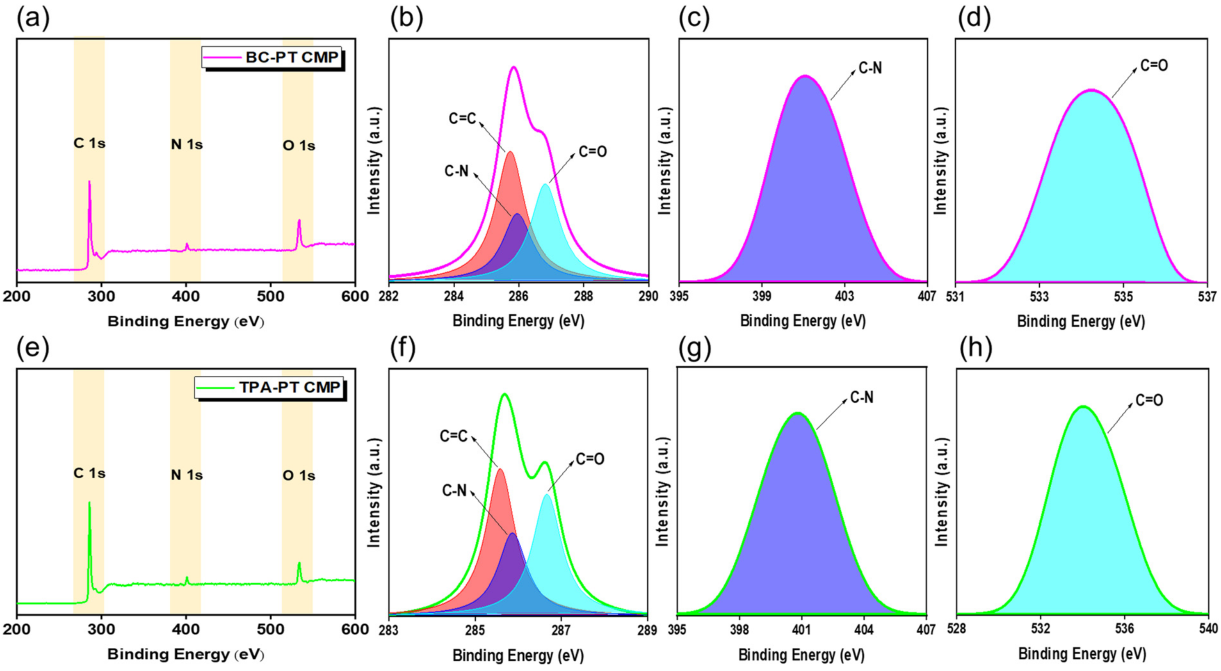

Fig. 2 XPS results of (a) BC-PT and (e) TPA-PT polymers. Peak fitting of (b) C 1s peak, (c) N 1s peak, and (d) O 1s peak of BC-PT; (f) C 1s peak, (g) N 1s peak, and (h) O 1s peak of TPA-PT CMPs.

for C 1s, N 1s and O 1s at 285.91, 401.55 and 533.42 eV, respectively, while the corresponding XPS signals for the TPA-PT CMP were 285.09, 400.73 and 534.15 eV, respectively. Fitting of the C 1s signal for BC-PT CMP produced three peaks at 285.74, 285.94 and 286.81 eV, which were attributed to C═C, C–N and C═O functional groups, respectively, while those corresponding to C 1s fitting peaks for TPA-PT polymer were basically located at 285.58, 285.85 and 286.66 eV, respectively (Fig. 2b and f). In addition, N 1s peak fitting for BC-PT and TPA-PT CMPs revealed only one peak for both of them at 401.07 and 400.77 eV, respectively, which were characteristic of C–N functionality (Fig. 2c and g). Moreover, O 1s signal fitting analysis resulted in peaks at 534.28 and 534 eV, which were assigned to the C═O functional group in BC-PT and TPA-PT CMPs, respectively (Fig. 2d and h).

XRD analysis of BC-PT and TPA-PT polymers demonstrated no observed diffraction peaks, which emphasized the amorphous nature of the prepared polymers (Fig. S5, ESI†), as reported for other CMPs.[50,51]

Fig. 3 represents the morphological structures of the PT-based CMPs obtained using SEM and TEM microscopic techniques. As shown in the SEM images (Fig. 3a and e), the BC-PT CMP displayed the presence of aggregated irregular tiny particles that were randomly distributed throughout its skeleton, whereas TPA-PT CMP possessed a condensed sponge-like morphology. In addition, the elemental mapping extracted from the energy-dispersive X-ray spectroscopy (EDS) identified the coexistence of carbon, nitrogen, and oxygen atoms, which were symmetrically spread on the surface of BC-PT and TPA-PT CMPs (Fig. 3b–d and f–h, respectively). TEM images featured disordered structures (Fig. 3i and k), while the corresponding images of the low-magnification HR-TEM demonstrated that the two polymers consisted of porous network structures (Fig. 3j and l). Upon preparation, and multiple purifications of our polymers, the amount of Pd residue was quantified using various methods including SEM-EDS mapping and TEM-EDX. All results confirmed that the Pd concentration in the BC-PT polymer was slightly higher than that of the TPA-PT polymer. The SEM-EDS elemental mapping revealed the existence of C, N, O and Pd atoms, which were homogeneously distributed over the polymers' surface with Pd contents of 1.14% and 0.84% for BC-PT and TPA-PT polymers, respectively (Fig. S6 and S7, ESI†). In addition, TEM-EDX analysis indicated that the BC-PT and TPA-PT CMPs possessed a residual Pd of 1.39% and 1.10%, respectively (Fig. S8, ESI†). Moreover, the Pd concentration was determined using ICP-OES to be 3.016 ppm for BC-PT CMP and 2.158 ppm for TPA-PT CMP (Table S2, ESI†).

To emphasize the porous structure of the as-synthesized polymers, low-temperature nitrogen adsorption–desorption isotherms were obtained (Fig. 4 and Table 1). Based on the IUPAC classification, the obtained isothermal curves of BC-PT and TPA-PT CMPs follow the type II profile. In addition, there is a minimum N_2 gas adsorption at lower relative pressure ($P/P_0 <$ 0.1) but a sharp increase of gas adsorption at P/P_0 values greater than 0.9 (Fig. 4a). A typical BET model was applied to determine the surface areas and the total pore volumes of our CMPs, which were shown to be 478 $m^2\ g^{-1}$ and 0.44 $cm^3\ g^{-1}$, for the BC-PT CMP and 232 $m^2\ g^{-1}$ and 1.07 $cm^3\ g^{-1}$ for the TPA-PT CMP, respectively. By the application of the nonlocal density functional theory (NLDFT), the BC-PT and TPA-PT polymers

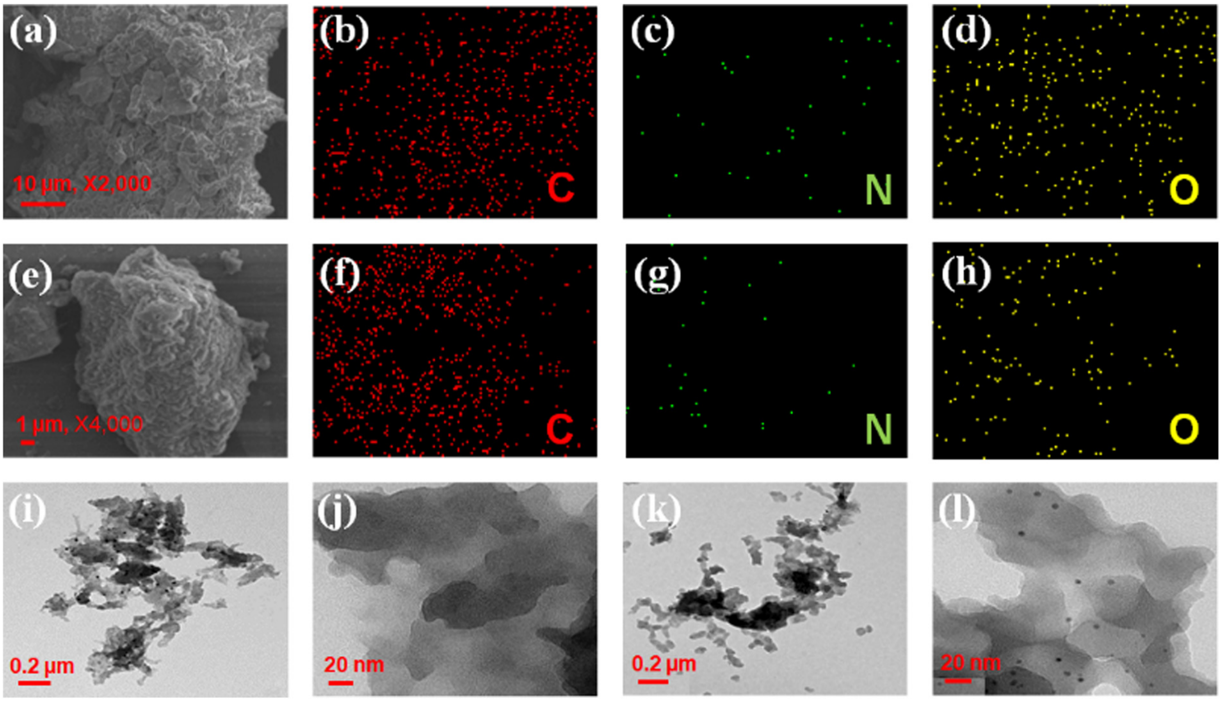

Fig. 3 SEM images of (a) BC-PT, and (e) TPA-PT CMPs. EDS elemental mapping photos (b–d) for BC-PT, and (f–h) for TPA-PT CMPs. TEM images of (i) and (j) for BC-PT, and (k) and (l) for TPA-PT CMPs.

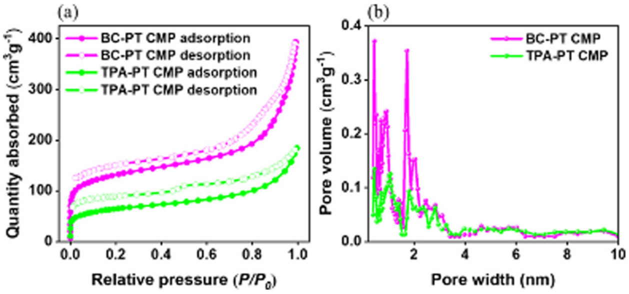

Fig. 4 (a) N_2 adsorption–desorption isotherms; (b) the corresponding pore size distribution curves of the BC-PT and TPA-PT CMPs.

Table 1 BET variables of the PT-linked polymers

CMPs	S_{BET} (m^2 g^{-1})	Pore size (nm)	Pore volume (cm^2 g^{-1})
BC-PT CMP	478	0.44	0.37
TPA-PT CMP	232	1.07	0.13

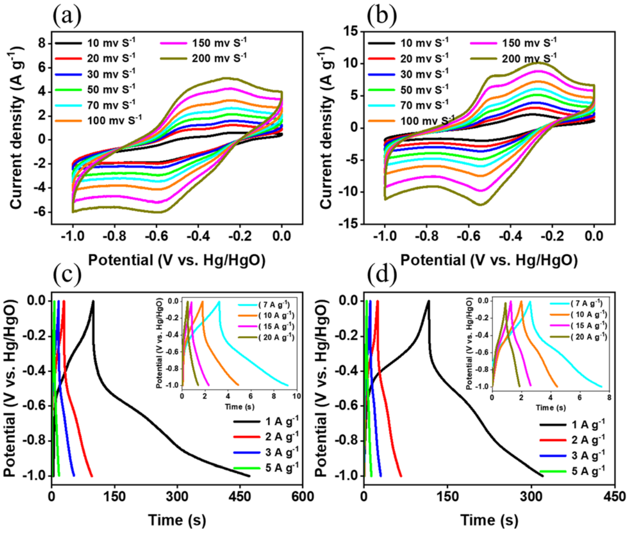

Fig. 5 CV curves of (a) BC-PT, and (b) TPA-PT CMPs. GCD curves of (c) BC-PT, and (d) TPA-PT CMPs, recorded at different current densities in a three-electrode system.

showed pore diameters of 0.44, and 1.96 nm, respectively (Fig. 4b).

Recently, numerous CMPs have been applied as efficient electrodes for energy storage devices[12,13] because of their outstanding advantages (for example, large surface areas, redox-active building blocks, and high physical and chemical stabilities). In this work, the electrochemical efficiency of the BC-PT and TPA-PT conjugated polymers was evaluated using CV and GCD profiles within a definite potential range (−1.0 to 0.0 V) and using the aqueous KOH electrolyte (1.0 M). The CV curves of our polymers were measured at specified scan rate potentials starting with 5 mV s^{-1} to the value of 200 mV s^{-1}, which possessed semi-rectangular shapes owing to the combined effect of EDLC and pseudocapacitance. At higher scan rates, the CV curves maintained their original shapes confirming the excellent stability and rate capability of the as-synthesized CMPs and proving the EDLC behavior[12] (Fig. 5a and b). The presence of the phenyl electrons besides the large surface areas of the carbonyl-rich CMPs led to great CV curve coherence over the whole scan rate potentials. Also, the abundance of nitrogen and oxygen atoms and the distinctive morphologies of our polymers significantly enhanced their pseudocapacitance, and the facile electron mobility improved the contact with the electrolyte. Moreover, the increasing of current densities by raising the potential sweep rates from 5 to 200 mV s^{-1} showed no changes in the semi-rectangular CV shapes, referring to fast kinetics and high-rate capability.[52]

The electrochemical storage properties of SCs are influenced by both EDLC and faradaic redox reactions. In the CV analysis of our PT-based CMPs, we observed two prominent redox peaks in each case. BC-PT CMP showed two redox peaks at −0.62/−0.58 V and −0.29/−0.21 V while TPA-PT CMP showed peaks at −0.62/−0.59 V and −0.19/−0.18 V against Hg/HgO due to presence of sufficient redox active carbonyl groups. These peaks indicate that redox processes significantly contribute to the capacitance of these materials. To further clarify this point, the presence of these redox peaks demonstrates that the PT-based CMPs undergo reversible redox reactions during the charge–discharge cycles, enhancing their overall capacitance. The specific potentials at which these redoxes occur suggest that certain functional groups within the PT framework are actively participating in the electrochemical process. This behavior is characteristic of faradaic reactions, where electron transfer occurs between the electrode and the electroactive species in the polymer.

At a specific range of current densities (1.0–10 A g^{-1}), triangular shapes for GCD curves with little curvature were obtained for both BC-PT and TPA-PT polymers, demonstrating the pseudocapacitive as well as the EDLC behavior.[53] (Fig. 5c and d) The specific capacities of the BC-PT and TPA-PT CMPs at 1.0 A g^{-1} were 373 and 204 F g^{-1}, respectively (Fig. 6a).

The greater capacitance of BC-PT CMP can be explained in terms of its larger surface area (478 m^2 g^{-1}) compared to that of the TPA-PT polymer (232 m^2 g^{-1}), which would enhance the transfer of the electrolyte ions toward the surface of the electrode material that finally led to improving the electrochemical reactions. Furthermore, the highest planarity of the BC-PT CMP sheets compared to the TPA-PT CMP would promote electron transportation throughout its structure and hence enhance its electrochemical efficacy. The retention stabilities of these electrode polymers over 5000 cycles at constant current density (10 A g^{-1}) were assessed. The cyclic stability for the BC-PT and TPA-PT CMPs were measured to have values of 94.37 and 91.20%, respectively (Fig. 6b). Our two PT-linked CMP electrodes had excellent electrochemical performance compared to other porous organic materials (Table S3, ESI†). According to Ragone plots, the energy and power densities of the BC-PT CMP in the three-electrode system were 51.81 W h kg^{-1} and 500 W kg^{-1}, whereas those corresponding to the TPA-PT CMP were estimated to be 28.33 W h kg^{-1} and 500 W kg^{-1}, respectively (Fig. 6c).

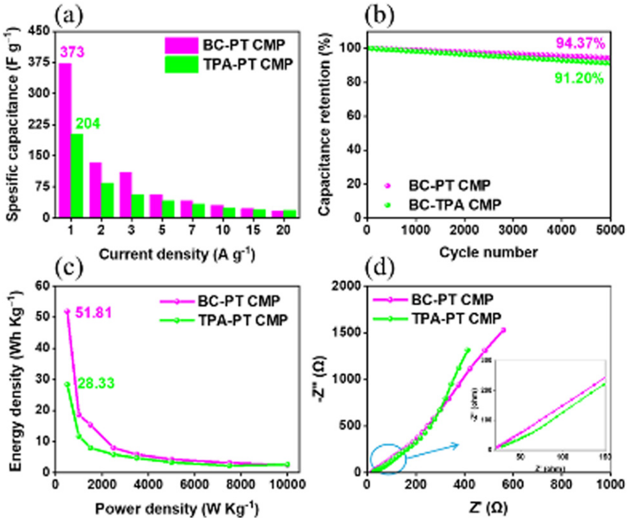

Fig. 6 (a) Specific capacitances of BC-PT and TPA-PT CMPs recorded at specific current densities (1.0 to 20 A g^{-1}). (b) Cycling stability at 10 A g^{-1} current density over 5000 cycles. (c) Ragone plots. (d) Nyquist plots of cells with the as-synthesized polymers in a three-electrode system.

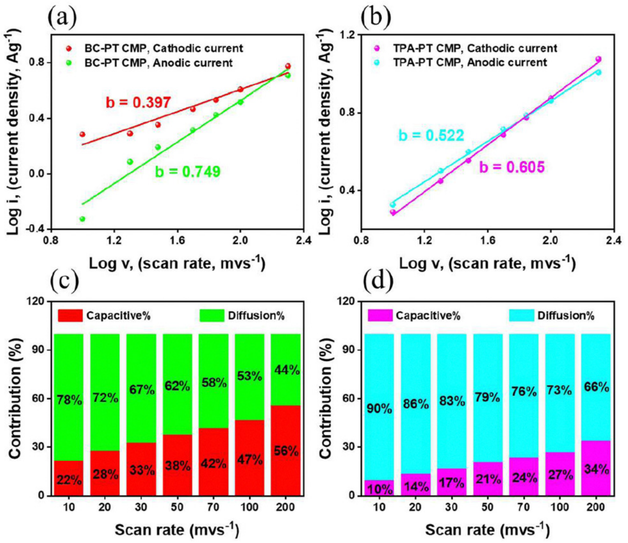

Fig. 7 (a) and (b) log(i) *versus* log(v) plots of (a) BC-PT, and (b) TPA-PT CMPs. (c) and (d) Relative contributions of the capacitive and diffusion-controlled energy storage of (c) BC-PT, and (d) TPA-PT polymers, measured at various scan rates.

We recorded the electrochemical impedance spectroscopy (EIS) of our polymers to find more information about the total interior resistance of the system. The Nyquist plots showed the resistance of the BC-PT and TPA-PT CMPs to be 22.7 and 28.1 Ω, respectively, offering smaller resistance and better capacitance for our materials (Fig. 6d).

The excellent capacitive behavior for the two porous materials was further confirmed using the frequency-dependent magnitude Bode plots, which showed negative slopes at smaller frequencies, and very small impedance at higher frequency ranges (Fig. S9a, ESI†). The knee frequency at a 45° phase angle (equal capacitance and resistance properties) was estimated using frequency-dependent phase-angle Bode plots for the as-prepared CMPs. The calculated knee frequencies for the BC-PT and TPA-PT CMPs were 159.35 and 56.26 Hz, respectively, suggesting their great performance for energy storage applications (Fig. S9b, ESI†).

Fig. S10 (ESI†) displays the Nyquist plots of both porous polymers obtained using EIS in the three-electrode system. The equivalent electric circuit includes components such as series resistance (R_s), charge transfer resistance (R_{ct}), constant phase elements for electric double layer capacitance (CPE-EDL) and pseudocapacitance (CPE-P) behavior, along with a Warburg element (Z_w), as shown in Fig. S10b (ESI†). The Nyquist plots were fitted using the above equivalent electric circuit which have been demonstrated in Fig. S10a (ESI†) as before and after fitting for the three-electrode SCs. The ohmic impedance was found to be 13.47 and 13.41 Ω for the BC-PT and TPA-PT, respectively.

The power law correlation (eqn (1)) between the current (i) and scan rate (v) was utilized to evaluate the capacitive and diffusive contributions of the BC-PT and TPA-PT CMPs in a three-electrode system.[54,55]

$$i = av^b \tag{1}$$

The factors "a" and "b" are constants, where "b" can be obtained by plotting log(i) against log(v). The BC-PT CMP exhibited b values of 0.749 and 0.397 for the anodic and cathodic currents, respectively, (Fig. 7a) while the b values of the TPA-PT polymer were 0.522 and 0.605 corresponding to the anodic and cathodic currents, respectively (Fig. 7b).

The percentage contribution can be calculated using the following eqn (2).[54,55]

$$i(V) = k_1v + k_2v^{1/2} \tag{2}$$

The percentage contributions of capacitance and diffusion at different scan rates are depicted in Fig. 7c and d. The results demonstrated that the BC-PT CMP had the capacitive contribution of 56% at 200 mV s^{-1}, which decreased to 22% at lower scan rate (10 mV s^{-1}). On the other hand, the TPA-PT polymer displayed 34% capacitive contribution, which diminished to 10% at the same corresponding scan rates. According to these findings, there is a coexistence of both capacitive and diffusion-controlled processes for storing energy using a three-electrode system.[56] The comparative contributions of these currents recorded at 10 mV s^{-1} are shown in Fig. S11 (ESI†). In addition, the greater capacitive contribution of the BC-PT polymer is comparable to that of the TPA-PT polymer which can be explained in terms of its accessible morphology and larger surface area.

For feasible implementation of the as-synthesized BC-PT polymer as a device, its electrochemical behavior of symmetric SCs (CR2032 coin cells) was evaluated, in which our CMP functioned as the cathode and anode within SSCs. We measured the CV curves at different scan rates (50 to 200 mV s^{-1}) and GCD profiles at various current densities (1.2–2.0 A g^{-1}). Almost all rectangular shapes of CV curves were obtained. Electrode coherence was observed at a higher sweep rate

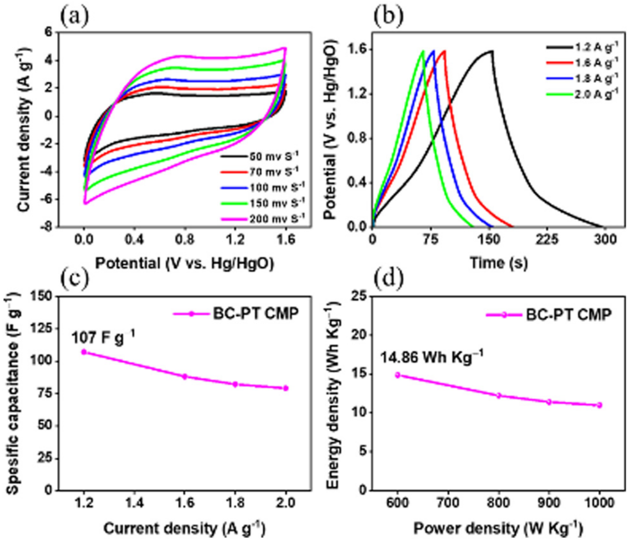

Fig. 8 (a) CV curves, (b) the corresponding GCD curves, (c) GCD specific capacitances recorded at different current densities, and (d) Ragone plot of the BC-PT CMP in the coin cell system.

Table 2 Comparison between the supercapacitive behaviour of the synthesized PT-based SSC device with other reported SSC devices

Electrode	Energy density (W h kg^{-1})	Power density (W kg^{-1})	Ref.
Try-Ph-Th CMP	7.3	250	57
Try-Ph-Py CMP	11.7	250	57
PANI/NCNT	11.1	980	58
FC-CMPs/rGO	8	124	59
PANI/MWNT	18	313	60
N-CNFs/900	7.11	125	61
N-PCNFs/PSN	8.5	250	62
MCSF porous material	9.6	108.5	63
IHPNC/carbon nanotubes	8.7	195	64
BC-PT CMP	**14.86**	**600**	**This work**

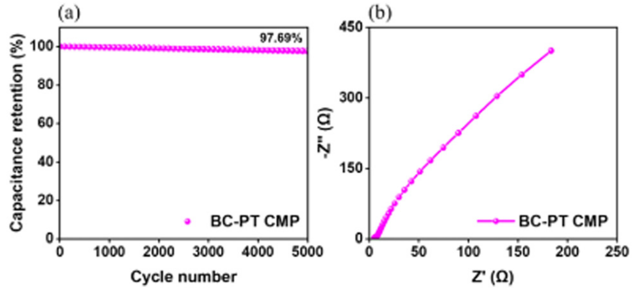

Fig. 9 (a) Cycling retention recorded at 10 A g^{-1} current density over 5000 cycles; (b) Nyquist plot of the BC-PT polymer in a coin cell.

potential providing enhanced rate capacities and kinetics as well (Fig. 8a).

Fig. 8b presents the GCD profiles of the BC-PT polymer which had an almost triangular shape with little curvature within the discharge process, affirming pseudocapacitive and EDLC behavior, consistent with the three-electrode system. Again, similar to the three-electrode system, the GCD discharge period was long compared to the corresponding charge period, emphasizing their suitability for practical utilization. Moreover, after the operation at specified current densities (1.2, 1.6, 1.8, and 2.0 A g^{-1}), the coin device with the BC-PT polymer demonstrated specific capacitances of 107, 88, 82 and 79 F g^{-1}, respectively (Fig. 8c). As shown in the Ragone plot (Fig. 8d), at a value of 600 W kg^{-1}, power density, the BC-PT achieved an excellent energy density of 14.86 W h kg^{-1}, which was a value comparable to other porous materials (Table 2). The stability measurements for our synthesized redox-active BC-PT polymer over 5000 cycles at fixed current density (10 A g^{-1}) were tested, and the long-term cycling stability was confirmed by providing capacity retentions of 97.69% (Fig. 9a). In addition, the EIS and Nyquist plots of the BC-PT CMP revealed that the internal resistance offered by its SSCs was 5.38 Ω, proving lower resistance and high conductivity of this polymer (Fig. 9b).

Furthermore, the frequency-dependent magnitude Bode plots were applied to determine the resistance behavior, and the frequency-dependent phase-angle Bode plots were utilized to investigate the knee frequencies for the BC-PT CMP. As represented in Fig. S12 (ESI†), this polymer exhibited a negative slope line at lower frequencies, minimum resistance at higher frequency range, and the estimated knee frequency at 45° phase angle was 105.83 Hz.

Fig. S13 (ESI†) also illustrates the Nyquist plots for the BC-PT CMP in a two-electrode system. The equivalent electric circuit utilized for fitting includes components such as R_s, R_{ct}, CPE-EDL, CPE-P and Z_w, as depicted in Fig. S13b (ESI†). The Nyquist plot was fitted using the equivalent electric circuit mentioned above, and the results are shown in Fig. S13a (ESI†) before and after fitting for the SC devices. In the case of a device, the ohmic resistance was significantly changed giving a value of 3.43 Ω. This value suggests that the porous polymer possesses high electrical conductivity and can be an ideal source as electrode materials for energy storage applications. In summary, the EIS analysis of this porous material reveals distinctive characteristics, demonstrating superior capacitive performance of BC-PT CMP. These findings highlight the importance of EIS in evaluating the electrical behavior of porous polymers and optimizing their performance in energy storage applications.

We performed calculations within the density functional theory (DFT) framework with the Gaussian package.[65] The B3LYP exchange–correlation functional[66–68] and the 6-31G basis set[69] were used. The calculations allow for describing and estimating structural and electrochemical characteristics of the utilized monomers and their corresponding polymers. After constructing the initial molecular geometries in Avogadro,[70] we performed full structure optimizations by DFT. The optimized geometries, highest occupied molecular orbitals (HOMOs), and lowest unoccupied molecular orbitals (LUMOs) of the monomers and their corresponding polymers are shown in Fig. S14 (ESI†). The optimized PT-2Br ($C_{16}H_4O_4Br_2$) is a planar molecule with a width and length of 0.719 and 1.098 nm, respectively, while BC-4BO ($C_{48}H_{60}O_8N_2B_4$) (width, depth and length are 1.291, 1.291 and 1.731 nm, respectively) and

TPA-4BO ($C_{54}H_{68}O_8N_2B_4$) (width, depth and length are 1.848, 0.590 and 1.874 nm, respectively) are not planar due to steric hindrances. We note that the moieties of the monomer building blocks maintain their structure in the polymer models confirming the rational behind the experimental synthesis strategy.

Our computational model of the BC-PT CMP ($C_{160}H_{72}O_{16}N_8$) is composed of four BC and four PT moieties and has a much larger size with a width of 4.032 nm, length of 3.166 nm and depth of 1.169 nm. The pore size was estimated at 2.429 and 2.463 nm. The model of the TPA-PT CMP ($C_{184}H_{104}O_{16}N_8$) consists of four linked PT and four TPA moieties. The optimized structure of the TPA-PT CMP has similar extensions of 3.771, 1.292 and 4.058 nm in width, depth and length, respectively, although the pore size has a more eccentric elliptical character with estimated half axes of 2.982 and 2.277 nm.

For computational insights into pseudo-capacitors, the total capacitance (C_T) can be written as the reciprocal values of the sum of the reciprocal contributions, such as the quantum capacitance (C_q), EDL capacitance (C_D) taken the form $1/C_T = 1/C_q + 1/C_D$. Our first principles calculation can shed light on some impact of the atomic structure on the resulting total capacitance using the Frontier orbitals, *i.e.* HOMO and LUMO, the density of states (DOS) and a computed estimate of the quantum capacitance. However, other factors and phenomena at the micro and mesoscale such as the kinetic relation between ions and pore sizes,[71–73] and material/electrolyte interface resistance can further impact C_D and C_T, which are beyond the scope of DFT. Nonetheless, properties such as DOS from first principles calculations can provide insights into possible effects linked to structural changes. Here we focus on C_Q because of the overall similarity of the two CMPs to reason for the observed differences in the capacitance. We adopted the computation $C_Q = e^2\int_{-\infty}^{\infty} D(E)F_T(E+\mu)\mathrm{d}E$ as used for semiconductors or graphene[74] where e is the charge of an electron, $D(E)$ is the density of states and energy E, the thermal broadening function $F_T(E,\mu) = \frac{1}{4kT}\mathrm{sech}^2\left(\frac{E-\mu}{2kT}\right)$ with k as Boltzmann constant, T as temperature, and $\mu = eU$ as the chemical potential relating to the applied electrode potential U. The computed C_q and DOS are given in Fig. S15 (ESI†).

The computed energy levels of the HOMO (ϵ_{HOMO}) of the TPA-PT and BC-TP polymers are rather different with −4.87 and −5.94 eV, respectively, while the LUMO energies (ϵ_{LUMO}) are very similar with about −3.7 eV. The LUMO in the TPA-PT polymer is localized and not distributed across the entire CMP unit, while the BC-PT polymer's LUMO is somewhat more delocalized at two locations in the polymeric system. The HOMO and LUMO orbitals are shown in Fig. S14b and e, S13c and f (ESI†), respectively. Still, the LUMOs in both CMPs are located at the PT moieties that contain the redox active carbonyl groups, while the HOMOs appear more delocalized and are located at the BC or TPA moieties. Since both CMPs appear similar in their LUMO energy and LUMO location, redox processes affecting the pseudo-capacitance should be similar, in particular, because it is expected that the electron insertion in redox processes is believed to occur at atoms associated with the LUMO,[75] although some contributions from electronic relaxation effects could occur causing some differences in the device performance as discussed for other organic redox-active compounds.[76] More distinct differences were observed for the quantum capacitance. For a given μ, the TPA-PT and BC-PT CMPs show district differences. The BC-PT shows significantly larger quantum capacitance for μ larger than −0.5 eV, while it is smaller for μ below −0.5 eV. Notably, the quantum capacitance at $\mu = 0$, *i.e.* an electrode potential of 0 V, is significantly (*i.e.* by a factor of 2.4) larger for the BC-PT than for the TPA-PT. Note that a dependence on the position of the Fermi energy remains. These differences result from their different electronic structures including the HOMO–LUMO gap, and the DOS extension beyond the frontier states for the given energy window. Hence, details in the electronic structure and in particular differences between TPA-PT's and BC-PT's C_Q could contribute to the experimentally observed different total capacitance.

The as-synthesized polymeric electrodes possessed remarkable electrochemical efficiency compared to other organic electrodes in literature. For example, the *in situ* polymerization of polytriphenylamine (PTPA) with MWCNT produced the PTPA@MWCNT, which displayed efficient electrochemical capacitance. The highest value was achieved up to 410 F g^{-1} in 0.5 M H_2SO_4 at a current density of 1.0 A g^{-1}, corresponding to PTPA@MWCNT-4. Its two-electrodes SC had a specific capacitance of 216 F g^{-1} and cyclic stability of 71% after 6000 GCD cycles.[77] Also, the MWCNT@SACMP composite, which has been synthesized by the Liao research group displayed a notable capacitance of 594 F g^{-1} when tested at a current density of 1.0 A g^{-1}, incorporating 10 wt% of MWCNTs. When a symmetric coin SC is constructed using MWCNT@SACMP, it demonstrates an effective electrochemical capacitance of 254 F g^{-1} with remarkable stability of 84.38% even after 6000 cycles.[78] In addition, the same research team has prepared solid-state symmetrical-twisted CNF@PTPA FSCs, which were confirmed to possess a great specific capacitance of 398 mF cm^{-2} with a great energy density of 18.33 μW h cm^{-2} for utilization as flexible wearable devices for storing energy.[79] Moreover, the polyaminoanthraquinone-based CMPs (PAQ) have been synthesized by the Thomas team through Buchwald–Hartwig coupling polymerization. The PAQs demonstrate an electrochemical capacitance of 576 F g^{-1} using 0.5 M H_2SO_4 in a three-electrode cell at a current density of 1.0 A g^{-1}. Impressively, they retain approximately 80–85% of their initial capacitances after 6000 cycles. Asymmetric coin SCs with PAQs represent a capacitance of 168 F g^{-1} and an energy density of 60 W h kg^{-1} at a power density of 1300 W kg^{-1} within a potential range of 0–1.6 V.[80]

Conclusions

In summary, we have provided a simple Suzuki coupling reaction to construct two 2D-CMPs bearing the 2,7-dibromopyrene-4,5,9,10-tetraone redox-active building block and examined their electrochemical performance as organic electrodes for SCs. The BC-PT CMP was a more appropriate organic electrode for storing energy owing to its chemical composition, higher porosity, and effective pi-pi stacking in both bicarbazole and pyrenone units, which led to capacitance efficiency and great conductivity as well. After measuring their electrochemical performance in a three-electrode system, the BC-PT CMP showed superb electrochemical efficiency with an apparent specific capacitance of 373 F g^{-1} at 1.0 A g^{-1}, along with higher GCD cyclic stability reaching 94.37% after 5000 cycles at 10 A g^{-1}. Furthermore, an outstanding energy density was observed to be 51.81 W h kg^{-1} at 500 W kg^{-1} power density, corresponding to the BC-TP CMP. Moreover, a two-electrode system with the BC-PT CMP displayed a prime capacitance (107 F g^{-1}) at 1.2 A g^{-1}, a high stability retention (97.69%) over 5000 cycles at 10 A g^{-1}, and an outstanding energy density (14.86 W h kg^{-1}) at 600 W kg^{-1} power density. The BC-PT CMP was better than TPA-PT CMP as the electrode material because of its larger surface area, bigger pore volume, greater planarity, and high conductivity.

Data availability

Data are contained within the article or ESI.†

Conflicts of interest

There are no conflicts to declare.

Acknowledgements

This study was supported financially by the National Science and Technology Council, Taiwan, under contract 113-2218-E-110-004- and 112-2221-E-110-005-MY3. Also, we thank the National Center for High-performance Computing (NCHC) for providing computational and storage resources.

Notes and references

1 S. Xiong, J. Liu, Y. Wang, X. Wang, J. Chu, R. Zhang, M. Gong and B. Wu, *J. Appl. Polym. Sci.*, 2022, **139**, 51510.

2 N. N. Loganathan, V. Perumal, B. R. Pandian, R. Atchudan, T. N. J. I. Edison and M. Ovinis, *J. Energy Storage*, 2022, **49**, 104149.

3 D. Zhao, H. Wang, Y. Bai, H. Yang, H. Song and B. Li, *Polymers*, 2023, **15**, 213.

4 S. Sahoo, R. Kumar, E. Joanni, R. K. Singh and J. S. Shim, *J. Mater. Chem. A*, 2022, **10**, 13190–13240.

5 C. Han, J. Tong, X. Tang, D. Zhou, H. Duan, B. Li and G. Wang, *ACS Appl. Mater. Interfaces*, 2020, **12**, 10479–10489.

6 Z. Ahmad, S. Kumar, C. K. Trinh, J. J. Shim and J. S. Lee, *Appl. Surf. Sci.*, 2023, **610**, 155464.

7 Z. Ahmad, W. B. Kim, S. Kumar, T. H. Yoon and J. S. Lee, *Electrochim. Acta*, 2022, **415**, 140243.

8 N. S. Shaikh, S. B. Ubale, V. J. Mane, J. S. Shaikh, V. C. Lokhande, S. Praserthdam, C. D. Lokhande and P. Kanjanaboos, *J. Alloys Compd.*, 2022, **893**, 161998.

9 H. Çınar and I. Kandemir, *Aerospace*, 2021, **8**, 85.

10 S. Zheng, Y. Sun, H. Xue, P. Braunstein, W. Huang and H. Pang, *Nat. Sci. Rev.*, 2022, **9**, nwab197.

11 S. Liu, L. Kang, J. Zhang, S. C. Jun and Y. Yamauchi, *ACS Energy Lett.*, 2021, **6**, 4127–4154.

12 A. F. Saber, S. W. Kuo and A. F. M. EL-Mahdy, *J. Mater. Chem. A*, 2024, **12**, 15373–15385.

13 A. F. Saber, S. U. Sharma, J. T. Lee, A. F. M. EL-Mahdy and S. W. Kuo, *Polymer*, 2022, **254**, 125070.

14 E. S. Shin, J. Y. Go, G. S. Ryu, A. Liu and Y. Y. Noh, *ACS Appl. Mater. Interfaces*, 2021, **13**, 4278–4283.

15 A. F. Saber, C. C. Chueh, M. Rashad, S. W. Kuo and A. F. M. EL-Mahdy, *Mater. Today Sustainability*, 2023, **23**, 100429.

16 A. F. Saber, A. M. Elewa, H. H. Chou and A. F. M. EL-Mahdy, *ChemCatChem*, 2023, **15**, e202201287.

17 J. X. Jiang, F. Su, A. Trewin, C. D. Wood, H. Niu, J. T. A. Jones, Y. Z. Khimyak and A. I. Cooper, *J. Am. Chem. Soc.*, 2008, **130**, 7710–7720.

18 A. I. Cooper, *Adv. Mater.*, 2009, **21**, 1291–1295.

19 C. G. López-Calixto, S. Cabrera, R. Pérez-Ruiz, M. Barawi, J. Alemán, V. A. de la Peña O'Shea and M. Liras, *Appl. Catal., B*, 2019, **258**, 117933.

20 J. Dong, K. Zhang, X. Li, Y. Qian, H. Zhu, D. Yuan, Q. H. Xu, J. Jiang and D. Zhao, *Nat. Commun.*, 2017, **8**, 1142.

21 M. Liras, M. Iglesias and F. Sánchez, *Macromolecules*, 2016, **49**, 1666–1673.

22 X. Gao, C. Shu, C. Zhang, W. Ma, S. B. Ren, F. Wang, Y. Chen, J. H. Zeng and J. X. Jiang, *J. Mater. Chem. A*, 2020, **8**, 2404–2411.

23 K. Lin, Z. Wang, Z. Hu, P. Luo, X. Yang, X. Zhang, M. Rafiq, F. Huang and Y. Cao, *J. Mater. Chem. A*, 2019, **7**, 19087–19093.

24 B. Bonillo, R. S. Sprick and A. I. Cooper, *Chem. Mater.*, 2016, **28**, 3469–3480.

25 Q. Liu, G. Li, Z. Tang, L. Chen, B. Liao, B. Ou, Z. Zhou and H. Zhou, *Mater. Chem. Phys.*, 2017, **186**, 11–18.

26 M. Trunk and J. F. Teichert, *J. Am. Chem. Soc.*, 2017, **139**, 3615–3618.

27 Q. Zhang, S. Yu, Q. Wang, Q. Xiao, Y. Yue and S. Ren, *Macromol. Rapid Commun.*, 2017, **38**, 1700445.

28 P. Pandey, A. P. Katsoulidis, I. Eryazici, Y. Wu, M. G. Kanatzidis and S. T. Nguyen, *Chem. Mater.*, 2010, **22**, 4974–4979.

29 C. Xu and N. Hedin, *J. Mater. Chem. A*, 2013, **1**, 3406–3414.

30 Y. Zhang, A. Sigen, Y. Zou, X. Luo, Z. Li, H. Xia, X. Liu and Y. Mu, *J. Mater. Chem. A*, 2014, **2**, 13422–13430.

31 V. Briega-Martos, A. Ferre-Vilaplana, A. de la Peña, J. L. Segura, F. Zamora, J. M. Feliu and E. Herrero, *ACS Catal.*, 2017, **7**, 1015–1024.

32 A. B. Marco, D. Cortizo-Lacalle, I. Perez-Miqueo, G. Valenti, A. Boni, J. Plas, K. Strutyński, S. De Feyter, F. Paolucci, M. Montes, A. N. Khlobystov, M. Melle-Franco and A. Mateo-Alonso, *Angew. Chem., Int. Ed.*, 2017, **129**, 7050–7055.

33 L. Wang, Y. Wan, Y. Ding, Y. Niu, Y. Xiong, X. Wu and H. Xu, *Nanoscale*, 2017, **9**, 4090–4096.

34 J. Kim, J. H. Kim and K. Ariga, *Joule*, 2017, **1**, 739–768.

35 R. R. Salunkhe, J. Tang, N. Kobayashi, J. Kim, Y. Ide, S. Tominaka, J. H. Kim and Y. Yamauchi, *Chem. Sci.*, 2016, **7**, 5704–5713.

36 Y. Shi and G. Yu, *Chem. Mater.*, 2016, **28**, 2466–2477.

37 A. F. Saber, K. Y. Chen, A. F. M. EL-Mahdy and S. W. Kuo, *J. Polym. Res.*, 2021, **28**, 1–12.

38 A. F. Saber, A. M. Elewa, H. H. Chou and A. F. M. EL-Mahdy, *Appl. Catal., B*, 2022, **316**, 121624.

39 X. Liu, Y. Xu and D. Jiang, *J. Am. Chem. Soc.*, 2012, **134**, 8738–8741.

40 A. F. Saber and A. F. M. EL-Mahdy, *New J. Chem.*, 2021, **45**, 21834–21843.

41 L. Chen, Y. Yang and D. Jiang, *J. Am. Chem. Soc.*, 2010, **132**, 9138–9143.

42 A. F. Saber, M. Ahmed, S. W. Kuo and A. F. M. EL-Mahdy, *Polym. Chem.*, 2023, **14**, 4079–4088.

43 J. Hu, D. Zhang and F. W. Harris, *J. Org. Chem.*, 2005, **70**, 707–708.

44 H. Cui, P. Hu, Y. Zhang, W. Huang and A. Li, *ChemElectroChem*, 2021, **8**, 352–359.

45 Y. Liang, P. Zhang and J. Chen, *Chem. Sci.*, 2013, **4**, 1330–1337.

46 T. Nokami, T. Matsuo, Y. Inatomi, N. Hojo, T. Tsukagoshi, H. Yoshizawa, A. Shimizu, H. Kuramoto, K. Komae, H. Tsuyama and J. I. Yoshida, *J. Am. Chem. Soc.*, 2012, **134**, 19694–19700.

47 S. Zheng, L. Miao, T. Sun, L. Li, T. Ma, J. Bao, Z. Tao and J. Chen, *J. Mater. Chem. A*, 2021, **9**, 2700–2705.

48 N. Wang, X. Bao, Y. Yan, D. Ouyang, M. Sun, V. A. L. Roy, C. S. Lee and R. Yang, *Polym. Chem.*, 2014, **52**, 3198–3204.

49 C. L. Chang, A. M. Elewa, J. H. Wang, H. H. Chou and A. F. M. EL-Mahdy, *Microporous Mesoporous Mater.*, 2022, **345**, 112258.

50 J. S. M. Lee and A. I. Cooper, *Chem. Rev.*, 2020, **120**, 2171–2214.

51 Q. Sheng, X. Zhong, Q. Shang, Y. Y. Dong, J. Zhao, Y. Du and Y. Xie, *Front. Chem.*, 2022, **10**, 854018.

52 A. M. Khattak, Z. A. Ghazi, B. Liang, N. A. Khan, A. Iqbal, L. Li and Z. Tang, *J. Mater. Chem. A*, 2016, **4**, 16312–16317.

53 C. Sengottaiyan, R. Jayavel, R. G. Shrestha, T. Subramani, S. Maji, J. H. Kim, J. P. Hill, K. Ariga and L. K. Shrestha, *Bull. Chem. Soc. Jpn.*, 2019, **92**, 521–528.

54 Q. Li, W. Lu, Z. Li, J. Ning, Y. Zhong and Y. Hu, *Chem. Eng. J.*, 2020, **380**, 122544.

55 W. Lu, J. Shen, P. Zhang, Y. Zhong, Y. Hu and X. W. Lou, *Angew. Chem., Int. Ed.*, 2019, **58**, 15441–15447.

56 E. Lim, C. Jo, H. Kim, M. H. Kim, Y. Mun, J. Chun, Y. Ye, J. Hwang, K. S. Ha, K. C. Roh, K. Kang, S. Yoon and J. Lee, *ACS Nano*, 2015, **9**, 7497–7505.

57 T. H. Weng, M. G. Mohamed, S. U. Sharma, S. V. Chaganti, M. M. Samy, J. T. Lee and S. W. Kuo, *ACS Appl. Energy Mater.*, 2022, **5**, 14239–14249.

58 R. Malik, L. Zhang, C. McConnell, M. Schott, Y. Y. Hsieh, R. Noga, N. T. Alvarez and V. Shanov, *Carbon*, 2017, **116**, 579–590.

59 A. M. Khattak, H. Sin, Z. A. Ghazi, X. He, B. Liang, N. A. Khan, H. R. Alanagh, A. Iqbal, L. Li and Z. Tang, *J. Mater. Chem. A*, 2018, **6**, 18827–18832.

60 B. S. Singu, P. Srinivasan and K. R. Yoon, *J. Solid State Electrochem.*, 2016, **20**, 3447–3457.

61 L. F. Chen, X. D. Zhang, H. W. Liang, M. G. Kong, Q. F. Guan, P. Chen, Z. Y. Wu and S. H. Yu, *ACS Nano*, 2012, **6**, 7092–7102.

62 Q. S. Meng, K. Q. Qin, L. Y. Ma, C. N. He, E. Z. Liu, F. He, C. S. Shi, Q. Y. Li, J. J. Li and N. Q. Zhao, *ACS Appl. Mater. Interfaces*, 2017, **9**, 30832–30839.

63 Q. Wang, J. Yan, T. Wei, J. Feng, Y. M. Ren, Z. J. Fan, M. L. Zhang and X. Y. Jing, *Carbon*, 2013, **60**, 481–487.

64 S. X. Zuo, J. Chen, W. J. Liu, X. Z. Li, Y. Kong, C. Yao and Y. S. Fu, *Carbon*, 2018, **129**, 199–206.

65 M. J. Frisch, G. W. Trucks, H. B. Schlegel, G. E. Scuseria, M. A. Robb, J. R. Cheeseman, G. Scalmani, V. Barone, G. A. Petersson, H. Nakatsuji, X. Li, M. Caricato, A. V. Marenich, J. Bloino, B. G. Janesko, R. Gomperts, B. Mennucci and J. B. H. Hratch, *Gaussian 16 Revision C.01*, Gaussian Inc., Wallingford CT, 2016.

66 A. D. Becke, *J. Chem. Phys.*, 1993, **98**, 5648–5652.

67 C. Lee, W. Yang and R. G. Parr, *Phys. Rev. B: Condens. Matter Mater. Phys.*, 1988, **37**, 785–789.

68 S. H. Vosko, L. Wilk and M. Nusair, *Can. J. Phys.*, 1980, **58**, 1200–1211.

69 B. P. Pritchard, D. Altarawy, B. Didier, T. D. Gibson and T. L. Windus, *J. Chem. Inf. Model.*, 2019, **59**, 4814–4820.

70 M. D. Hanwell, D. E. Curtis, D. C. Lonie, T. Vandermeersch, E. Zurek and G. R. Hutchison, *J. Cheminf.*, 2012, **4**, 17.

71 K. G. Latham and S. W. Donne, *J. Electrochem. Soc.*, 2018, **165**, A2840–A2848.

72 M. Zhang, C. Yang, Y. Wang, F. Gao, J. Cheng and J. Zhang, *J. Electrochem. Soc.*, 2018, **165**, A3313–A3320.

73 B. A. Ali and N. K. Allam, *Phys. Chem. Chem. Phys.*, 2019, **21**, 17494–17511.

74 E. Paek, A. J. Pak, K. E. Kweon and G. S. Hwang, *J. Phys. Chem. C*, 2013, **117**, 5610–5616.

75 K. Fukui, *Theory of Orientation and Stereo selection*, Springer, Berlin, 1970, pp. 1–85.

76 J. Lüder and S. Manzhos, *Front. Chem.*, 2020, **8**, 83.

77 H. Zuo, J. Duan, B. Lyu, W. Lyu, Y. Li, X. Mei and W. Liao, *Macromol. Rapid Commun.*, 2023, **45**, 2300238.

78 W. Lyu, C. Yan, Z. Chen, J. Chen, H. Zuo, L. Teng, H. Liu, L. Wang and Y. Liao, *ACS Appl. Energy Mater.*, 2022, **5**, 3706–3714.

79 W. Lyu, W. Zhang, H. Liu, Y. Liu, H. Zuo, C. Yan, C. F. J. Faul, A. Thomas, M. Zhu and Y. Liao, *Chem. Mater.*, 2020, **32**, 8276–8285.

80 Y. Liao, H. Wang, M. Zhu and A. Thomas, *Adv. Mater.*, 2018, **30**, 1705710.